


Control of leading-edge separation on bioinspired airfoil with fluttering covertsXingyu Ma ^{1,2,3,*} Xuan Gong,^{1,2,3} Zhanqi Tang,^{1,2} and Nan Jiang^{1,2}¹*Department of Mechanics, School of Mechanical Engineering, Tianjin University, Tianjin 300350, China*²*Tianjin Key Laboratory of Modern Engineering Mechanics, Tianjin 300350, China*³*China Key Laboratory of Aerodynamic Noise Control, China Aerodynamics Research and Development Center, Mianyang 621000, China*

(Received 19 August 2021; accepted 26 January 2022; published 17 February 2022)

In this work, the aerodynamic role of the artificial covert feathers (i.e., coverts) on an airfoil is experimentally studied in a wind tunnel to investigate the flow control effect on the leading-edge separation. We apply flexible featherlike devices on a high-angle-of-attack airfoil. We use a hot-wire anemometer to measure the velocity profiles and turbulent fluctuations in the downstream wake flow. As a baseline of flow separation, a two-dimensional NACA 0018 airfoil model is set at the angle of attack of 15° at the chord-based Reynolds number of 1.0×10^5 , causing strong leading-edge and trailing-edge shear layers and a low-speed wake flow area in between as large as 0.35 chord length. When deployed on the upper wing surface, the flexible coverts adaptively flutter under the influence of the local unsteady airflow. Hot-wire measurement results show that the leading-edge coverts effectively suppress the flow separation and reduce the size of the wake flow area. The change of power spectral density shows that the predominant peaks as the fundamental and harmonic frequencies are both attenuated due to the suppression of unsteady motions of the shear layers. On the other hand, the fluttering coverts at the trailing edge modify the trailing-edge shear layer by redistributing the turbulent kinetic energy to the high-frequency components. By simultaneous double-point measurement, we find that the leading-edge and trailing-edge shear layers are drawn closer to each other, and the two shear layers show an increased peak in the coherence spectrum. Further multiscale wavelet analysis shows that the perturbations at the 60% chord length increase the large-scale amplitude modulation of small-scale turbulence and therefore they stabilize the leading-edge and trailing-edge shear layers. Meanwhile, the flow intermittency outside of the wake flow area is attenuated as well. The effective flow control effects in the present work are in good agreement with the previous direct observations of bird flight in literature that the coverts on the upper wing surface play an important role in flow separation control during high-angle-of-attack flight. These findings advance the understanding of aerodynamic contribution of the covers on bird wings and reveal the engineering potential of bioinspired coverts for flow separation control of aircrafts and unmanned air vehicles.

DOI: [10.1103/PhysRevE.105.025107](https://doi.org/10.1103/PhysRevE.105.025107)**I. INTRODUCTION**

Birds have shown sophisticated skills of flying by efficiently utilizing natural wind and controlling the airflow around the wings, especially during gliding and soaring when their wings are kept outspread and steady without much flapping motion. A recent study reported that an Andean condor, as a large and heavy raptor, can sustain gliding and soaring by flapping for only 1% of their flight time under various environmental conditions [1]. During the steady-state gliding and soaring flights, feathers play a significant role in forming the wing profile and guiding the airflow around the wing surfaces. There are two approaches for the feathered wings to achieve amazing aerodynamic efficiency and robustness by interacting with the surrounding airflow. The first is an active and purposeful method by which the primary feather configurations, including the sweep, span, and contour [2–8], are ingeniously morphed in response to continuously changing flow conditions or by elevating the alulae to induce leading-edge vortices for generating higher lift [9,10]. The other one

is a passive and robust method in which the flexible coverts adaptively deflect and flutter at the tips under the influence of the separated airflow, particularly when the leading-edge flow separation occurs at high angles of attack [11–16], such as perching, landing, and gliding in a gust of wind. According to the early study of wing and feather structures, Brown *et al.* [11] found that the coverts which are exposed to airflow are associated with mechanoreceptors near the follicles. Acting like motion sensors, these mechanoreceptors simultaneously detect vibrations of the coverts for measuring airspeed and detecting an imminent flow separation on the wing surface. In their outdoor field tests, Carruthers *et al.* [10] proved the self-activation of the coverts in flight by installing a video camera on a free-flight steppe eagle. It is clearly observed that the tips of the coverts are passively deflected away from the wing surface when the steppe eagle set the wings at high angles of attack during the perching phases. Further experimental evidences reported by Bachmann *et al.* [13] showed that generic feather flexural stiffness mainly depends on the geometry of the feathers rather than on the elastic modulus (Young's modulus). Although numerous studies have been carried out on bird wing morphology [2,7], flight kinematics [3,5,15,16], and feather configurations [6,9], few studies focus

*Corresponding author: xingyuma@tju.edu.cn

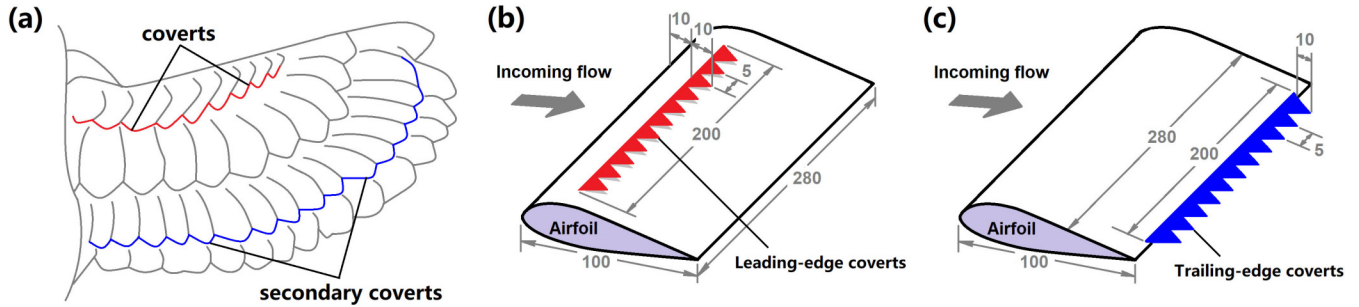


FIG. 1. Schematic of the experimental setup. (a) Illustration of the coverts (red) and the secondary coverts (blue) on the upper surface of a bird wing. (b) Leading-edge coverts (red) deployed at the 10% chord length; (d) trailing-edge coverts (blue) deployed at the 100% chord length.

on the aerodynamic contribution of the fluttering coverts on bird wings.

As inspired by the coverts on bird wings, researchers have carried out experimental and numerical studies of artificial flaps for the flow separation control of high-angle-of-attack wings [12,17–22]. One of the typical designs is where the rigid flaps are hinged at the root on the upper wing surface with the tips freely deflected. When the leading-edge separation occurs, the flaps are adaptively activated by the reversed flow, resulting in modification of the separation bubble and the shedding vortices [5]. In early studies, Bramesfeld and Maughmer [17] reported that, compared to the clean wing, the bioinspired flap hinged at the 86% chord length increases the maximum lift coefficient by approximately 20%. This improvement is mainly attributed to a reduction of the upper-surface pressures that occur upstream of the flap, which can be regarded as a “pressure dam” that reduces the adverse effects of the separation on the pressure distribution of the attached flow upstream. More importantly, this adaptive device is only self-activated by the local reverse flow on the upper wing surface and is otherwise attached to the wing surface. The effectiveness and adaptability of the artificial flap has been studied and supported by wind tunnel tests [19–21] and flight experiments [12,18]. A recent particle image velocimetry (PIV) measurement by Arivoli *et al.* [22] found that the flaps at the 60% and 80% chord lengths promote large-scale vortex formation and the flap-shear layer interaction increases the flow entrainment, which is responsible for the reattachment of the separated shear layer. Particularly, when the flap is deployed at the 60% chord length, the large separation bubble (referred to as the recirculation region) is divided into two small bubbles, namely, the leading-edge vortex (LEV) and the trailing-edge vortex (TEV), resulting in increased entrainment of the leading-edge shear layer and reduced turbulent fluctuations in the wake.

However, it is difficult for the rectangular single-degree-of-freedom rigid flap to simulate the behavior of feathers, because the real covert feathers on bird wings have barbules and serrated edges, and moreover, they are deformable at the tips to pop-up and flutter under the influence of the airflow. For studying the fluid-structure interaction between feathers and surrounding fluid flow, Favier *et al.* [23] numerically simulated the feather-coated circular cylinder and the resulting wake flow. The lock-in effect is found where

the feathers synchronize on the natural frequency of the surround flow and therefore cause stabilization of the wake. By a wind tunnel experiment, Klaen *et al.* [24] found that the featherlike coating on the upper wing surface promotes the leading-edge flow transition from laminar to turbulent flows, and therefore it reduces the size of the separation bubble in the wake. More recent studies by experiments [25] and numerical simulations [26,27] have shown that as the flexible flap on the upper wing surface flutters back and forth, in addition to the elevation of the whole feather vane, it follows the airflow and generates small-scale vortices in the proximity of the tips in addition to the LEV and TEV. Therefore the flexible flaps provide an effective method for flow separation control.

In this study we carry out wind tunnel tests on the leading-edge flow separation control effect of flexible serrated featherlike devices on a high-angle-of-attack wing model. The outline of the paper is arranged as follows. Section II; introduces the experimental models and hot-wire anemometer system. Section III describes the wavelet method for analyzing the multiscale velocity components in the turbulent flows. Section IV shows the measurement results in the time and frequency domains. The characteristic flow control effects of the fluttering coverts deployed at various positions are discussed. Finally, Sec. V; summarizes the results and proposes an outlook for future work.

II. EXPERIMENTAL METHODS

A. Wind model and flow control devices

The experiments were carried out in the low-speed open-circuit wind tunnel at Tianjin University. A two-dimensional NACA 0018 airfoil model (chord length $c = 100.0$ mm, wing span $s = 280.0$ mm) was installed in the center of the test section as shown in Figs. 1 and 2. The incoming free-stream velocity was $U_0 = 15.2$ m/s, with medium turbulent intensity of $I = 1.0\%$. So the Reynolds number was $Re = U_0 c / \nu = 1.0 \times 10^5$, based on the free-stream velocity, the chord length, and the kinematic viscosity of air at a room temperature of 20°C. The incoming flow condition and the Reynolds number were set within the generic range of medium-sized bird flights and low-Reynolds-number aircrafts [28]. During the measurements, the angle of attack was set at $\alpha = 15^\circ$, right above the critical angle of attack of a NACA 0018 airfoil

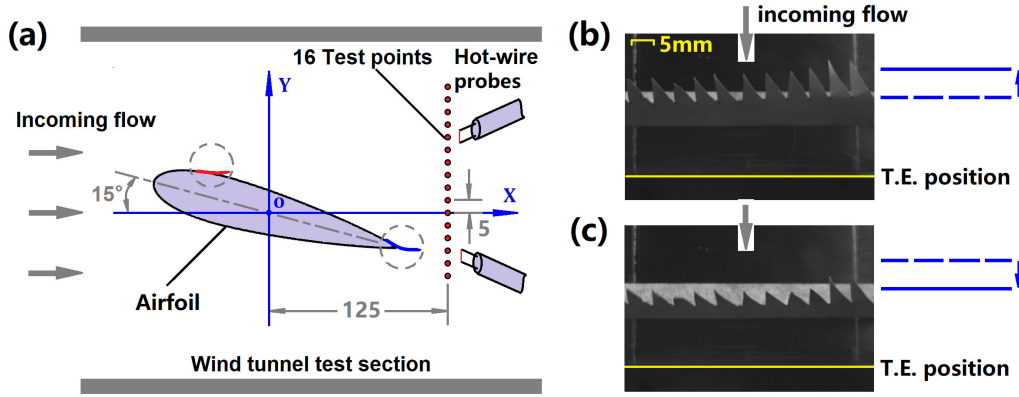


FIG. 2. Schematic of the wind tunnel experiments. (a) Schematic of the NACA 0018 airfoil model at 15° angle of attack and the 16 measurement points in the wake flow. The covers at the 10% and 100% chord lengths are circled for example. (b), (c) Photographs of the high and low positions of the fluttering covers deployed at the 80% chord length.

at this Reynolds number [29]. Therefore leading-edge flow separation occurs on this high-angle-of-attack wing model and this flow case is used as a baseline, denoted by the “clean wing” case. The flexible, serrated, and featherlike covers were made of a thin silicone membrane (thickness 0.10 mm; area density 7 mg/cm²; elastic modulus ~1 MPa). The device roots were fixed on the surface while the serrated tips were able to freely deflect or flutter, as shown by the photos in Figs. 2(b) and 2(c). In order to act like the covers near the leading edge and the secondary covers near the trailing edge, the device was deployed on the upper wing surface from the leading edge at 10%, 20%, and 40% of the chord lengths, as three leading-edge covers, and further at 60%, 80%, and 100% of the chord lengths, as three trailing-edge covers. The covert-deployed test cases are denoted by the respective positions. The dimensions and positions of the covert are listed in Table I. The Cartesian coordinate system was set in the center of the wing model as the origin, with the *x* and *y* axes in the streamwise and vertical directions, respectively.

B. Hot-wire measurements

The velocity of the wake flow field downstream of the wing model was measured by a TSI-IFA-300 hot-wire system as shown in Fig. 2(a). The hot-wire system consists of two TSI-1210-T1.5 single-sensor probes (material: tungsten; length: 1.25 mm; diameter: 4 μm), data acquisition system, and a PC control system. The hot-wire anemometer run in the constant temperature mode at an overheat ratio of 1.7 and the sampling rate was set at *f_s* = 5 kHz in order to obtain the small-scale turbulent fluctuations in the wake flow, in which the integral

timescale is approximately 0.002 s. In the present analysis, the nondimensional frequency is defined by the Strouhal number *St* ≡ *fc*/*U*₀, based on the chord length and the incoming free-stream velocity. Prior to the measurements, calibration was carried out by an air velocity calibrator in the velocity range of 0.5–25.0 m/s. The miniature probes were positioned in the wake flow normal to the flow direction by a high-precision positioning system (position accuracy: 0.01 mm). For each test case, single-point and double-point measurements were carried out, respectively:

(i) In single-point measurement, the single hot-wire probe was consecutively positioned at 16 points in the range of $-25.0 \leq y \leq 50.0$ mm with a constant spacing $\Delta y = 5.0$ mm along a vertical line at *x* = 125 mm downstream of the center of the wing model. By scanning the wake flow, the single-point measurement obtains the time-averaged velocity profile as well as rms distribution for evaluating the flow separation control effect. To reach the statistical convergence, the length of velocity data at each measurement point was 2.6×10^5 in the time duration of *T_s* = 52 s, which is as long as *T_s**U*₀/*c* = 8000 nondimensional characteristic time units. The high sampling frequency and long acquisition time enable one to resolve the small-scale turbulence and to obtain the energy convergence of the largest-scale flow structures.

(ii) In double-point measurement, on the other hand, the first probe was fixed at *y* = −10.0 mm within the trailing-edge shear layer as a reference, while the second probe scanned in seven points in a range of $0 \leq y \leq 30.0$ mm with the same spacing. It should be noted that the position of the first probe was fixed at the peak of the rms velocity profile based on the single-point measurement result. By simultaneously obtaining velocity data at two points, the double-point measurement therefore enables us to reveal the correlation and coherence between the leading-edge and trailing-edge shear layers.

III. WAVELET ANALYSIS METHODS

A. Wavelet decomposition and reconstruction

The wavelet analysis is a mathematical processing method for analyzing one-dimensional velocity data in the time-frequency domain. By decomposing the instantaneous into the

TABLE I. Dimensions and positions of the covers.

Test Case	Distance from the Leading Edge [mm]	
L.E. covers	10% <i>c</i>	10
	20% <i>c</i>	20
	40% <i>c</i>	40
T.E. covers	60% <i>c</i>	60
	80% <i>c</i>	80
	100% <i>c</i>	100

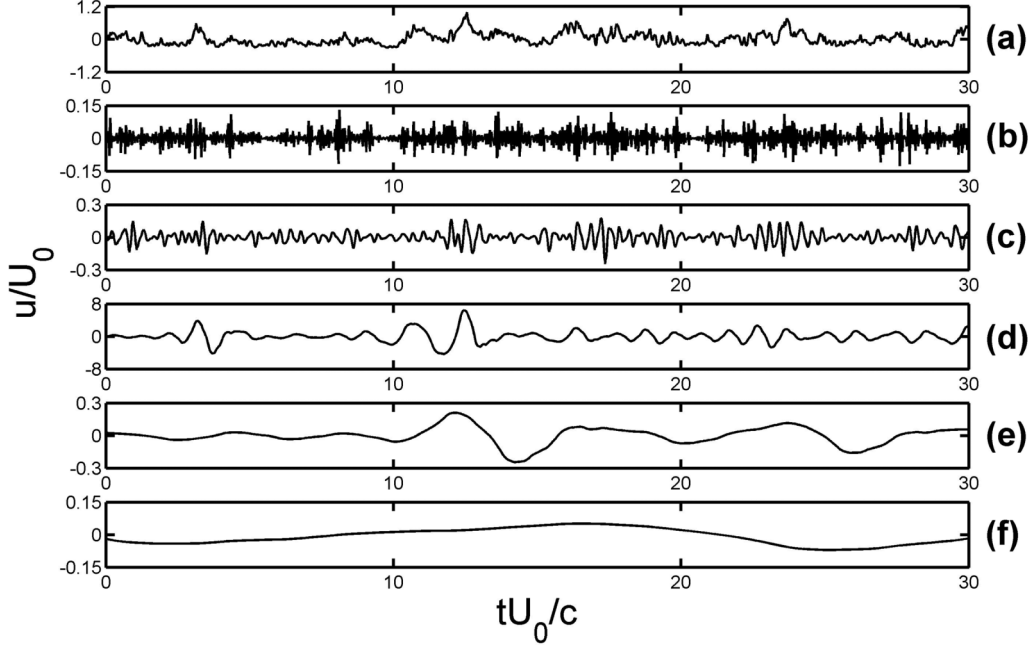


FIG. 3. A segment of instantaneous velocity data and the wavelet decompositions at different scales. (a) Measured data, (b) scale 1, (c) scale 3, (d) scale 5, (e) scale 7, and (f) scale 9. The measurement point is at $y/h = -0.1$ within the trailing-edge shear layer of the clean wing case. The time-averaged velocity is removed.

time-frequency space, it reveals the multiscale flow structures with different frequencies and their temporal evolution. An extensive review of the wavelet theory and applications to turbulence can be found in Farge [30]. More recent studies can refer to Meneveau [31], Watanabe *et al.* [32], Simoni *et al.* [33], Tang *et al.* [34], and He *et al.* [35]. Here we briefly introduce the algorithm of the one-dimensional discrete wavelet transform (DWT). The wavelet function $\Psi_{a,b}$ is obtained by scaling and shifting a mother wavelet “db5,” which is one of the most widely used functions of the Daubechies wavelet family [36,37]:

$$\Psi_{a,b}(t) = \frac{1}{\sqrt{a}} \Psi\left(\frac{t-b}{a}\right). \quad (1)$$

The parameters a and b are the scaling factor of size and translation along the time axis, respectively. Therefore the one-dimensional discrete wavelet transform is processed by convoluting the complex-conjugated wavelet function with the instantaneous velocity data as

$$W(a, b) = \sum_{t=1}^N u(t) \Psi_{a,b}^*(t). \quad (2)$$

The resulting wavelet coefficient matrix $W(a, b)$ is a function of the frequency and time. As in the discrete form, the scaling factor is set at ten levels and it exponentially grows as a power of 2. So a larger scaling factor corresponds to a lower frequency component, and vice versa. The i th scale is denoted by “scale i .” As a result, scale 1 corresponds to the maximum resolved frequency of $f_s/2 = 2500$ Hz, and scale 10 corresponds to the minimum resolved frequency of $f_s/2^{10} \approx 4.9$ Hz, which is sufficient to resolve low-frequency flow features in the wake. According to the Reynolds decomposition, the instantaneous velocity data can be decomposed

into the time-averaged value and a linear combination of wavelet reconstruction, which can be written in the matrix form as

$$u(t) = \bar{u} + D^T W, \quad (3)$$

in which the term D is the wavelet decomposition vector, which is orthonormal and contains ten levels of orthogonal wavelet bases. Figure 3 shows an example of the original measured data and its wavelet decompositions at $y/h = -0.1$ within the trailing-edge shear layer. The first row in Fig. 3(a) shows the instantaneous velocity data (without the time-averaged component). It contains strong intermittent velocity peaks and multiscale turbulent fluctuations. The following rows in Figs. 3(b)–3(f) show the wavelet decompositions of scale 1, scale 3, scale 5, scale 7, and scale 9 in ascending order of levels, respectively. It reveals that the separated shear layer contains not only the small-scale turbulent fluctuations but also the large-scale coherent structures in a wide range of nondimensional frequencies from $St = O(10)$ to $St = O(0.01)$. Therefore, based on the velocity triple decomposition, the unsteady velocity can be decomposed into large-scale coherent structure \bar{u} and small-scale turbulence u' as

$$u(t) = \bar{u} + \bar{u} + u' = \bar{u} + D_L^T W_L + D_S^T W_S. \quad (4)$$

The subscripts L and S represent the large-scale and small-scale components, respectively.

B. Amplitude modulation

Generally, amplitude modulation means the modulation of high-frequency data (usually referred to as the carrier waves) by a low-frequency data (modulating wave). For characterizing the interaction of the multiscale flow structures under the influence of the flow control devices, we analyze the

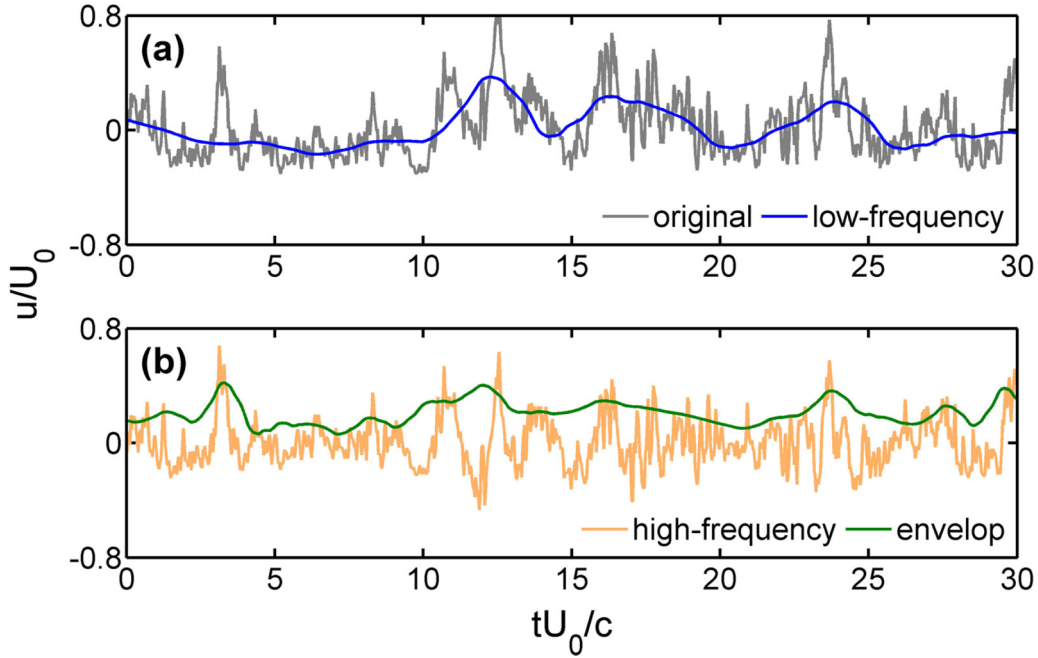


FIG. 4. A segment of instantaneous velocity data and its low- and high-frequency components at $y/h = -0.1$ within the trailing-edge shear layer. (a) Original data and the low-frequency component; (b) high-frequency component and its low-pass filtered envelop. The time-averaged velocity is removed.

amplitude modulation effects of the small-scale turbulence by the large-scale coherent structures. By selecting a proper scale as a criterion, the discrete wavelet transform can be used as a low-pass filter of velocity data. In this work we consider the wavelet reconstruction by the combination from scale 7 to scale 10 as the large-scale component \tilde{u} , while the rest of the scales is the small-scale component u' , in which the criterion is based on the power spectral distribution in the spectrum. Following the algorithm by Mathis *et al.* [38], we separate the instantaneous velocity data at each point into the large-scale and small-scale components with a cutoff frequency of $St = 0.26$. Then we calculate the envelop $E(u')$ of the small-scale component by the Hilbert transform and subsequently apply the wavelet low-pass filtering once more to obtain the low-pass filtered envelop $E_L(u')$. Therefore we cross-correlate the large-scale component and the low-pass filtered envelope of the small-scale component as

$$AM = \frac{\overline{\tilde{u}E_L(u')}}{\sqrt{\overline{\tilde{u}^2}}\sqrt{\overline{[E_L(u')]^2}}}. \quad (5)$$

The term AM is the cross-correlation coefficient within the range from -1 to 1, which is used as a normalized indicator to evaluate the amplitude modulation effect of the small-scale component by the large-scale component. Figure 4 provides an example of the same original velocity data as Fig. 3, the low- and high-frequency components, and the low-pass filtered envelop of the high-frequency component. In most of the previous studies in the literature, the Fourier transform filtering technique is usually used for scale separation with a fixed cutoff frequency. In this work, on the other hand, the wavelet multilevel reconstruction enables one to analyze the amplitude modulation of each scale of high-frequency components (from

scale 1 to scale 6), as well as a linear combination of them [35].

IV. RESULTS AND DISCUSSION

A. Flow control results

Figure 5 shows the leading-edge flow separation occurs over the clean wing at the angle of attack of 15° . This phenomenon is consistent with the literature [29]. As a result, the boundary layer flow near the leading edge separates from the upper wing surface and forms a separated shear layer, which is referred to as the leading-edge shear layer. Meanwhile, the one separating from the trailing edge is referred to as the trailing-edge shear layer. Both unsteady shear layers contain strong shear motions and shedding vortices, as visualized by the PIV measurements by Henningsson *et al.* [5]. By examining the rms velocity distribution of the clean wing, we find two distinctive peaks which indicate the positions of the leading-edge and trailing-edge shear layers at $y/c = 0.2$ and -0.15 , respectively. In between the two separated shear layers, there is the wake flow as large in size as half the chord length. The minimum velocity within the wake flow is approximately only 30% of the incoming flow velocity.

The modification of the time-averaged velocity profile is one of the most important indicators for evaluating flow separation control effect. By applying the flexible coverts near the leading edge at the 10% chord length, the time-averaged velocity deficit is considerably recovered and the two rms peaks of the shear layers merge into one, as shown in Fig. 5(b). The rms velocity peak is attenuated by 20.6% under the influence of the fluttering coverts. That means that the leading-edge flow separation is clearly suppressed, leading to considerable aerodynamic improvement in term of the lift and drag force

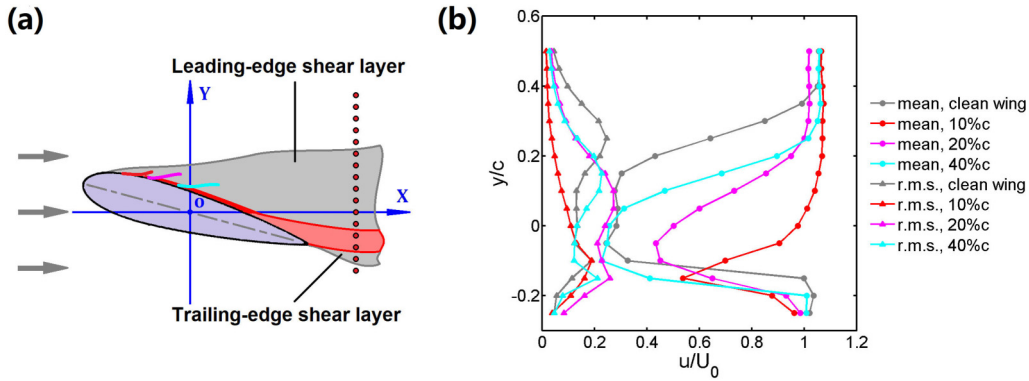


FIG. 5. (a) Schematic of the flow separation control effect by the leading-edge coverts at the angle of attack of 15°. The red area represents the reduced wake and the gray area is the baseline. (b) The time-averaged velocity profiles (dots) and rms velocity distributions (triangles) of the “10%c,” “20%c,” “40%c,” and the clean wing cases.

[18,19,25,27]. On the other hand, deploying the coverts at 20% or 40% chord lengths leads to a less effective result due to the position dependence. Direct observation during the wind tunnel test shows the free tips flutter rapidly driven by the airflow, acting like the covert feathers on a bird wing. Therefore they generate unsteady perturbations, with the rms velocity as much as $0.1 U_0$ to the boundary layer flow on the upper wing surface prior to the location, where it begins to separate from the wall due to the adverse pressure gradient. The covert-generated perturbations intrinsically increase the momentum transfer within the boundary layer, which promotes the boundary layer to overcome the adverse pressure gradient and remain attached along the entire upper wing surface [39,40]. Although the adaptive coverts generate perturbations just like the vortex generators, Carruthers *et al.* [10] described the difference between them: the former one is only activated when separation occurs while the later one generates perturbations all the time. Furthermore, unlike the vortex generators that increase turbulent fluctuations downstream [12,39], it is noteworthy that the fluttering coverts are driven to flutter by using the energy from the airflow, and in return, the resulting perturbations cause effective suppression of flow separation and significant reduction of turbulent kinetic in the wake flow.

In the following tests, Fig. 6 shows the flow separation control effects of the coverts near the trailing edge at the 60%, 80%, and 100% chord lengths. The time-averaged velocity profiles show that the leading-edge shear layer is drawn downward closer to the upper wing surface as a result of the coverts. Moreover, the rms peaks of the leading-edge and trailing-edge shear layers are decreased accordingly. The positions and peaks of the rms distributions in the clean wing and the flow control cases are listed in Table II. Among the three test cases, the 60%c case shows the most effective flow separation control result, and the turbulent kinetic energy within the leading-edge and trailing-edge shear layers are reduced by 12% and 30%, respectively. According to the vortex topological analysis in the previous studies [22,25], the trailing-edge coverts block the reversed flow near the wall and divide the large separation bubble into two small bubbles. Meanwhile, the fluttering motions generate unsteady perturbations in the proximity of the tips that may influence the dynamics of the LEV and TEV [15,25]. Although the velocity deficit in the wake flow is not recovered as much as that of the leading-edge coverts in Fig. 5(b), it is interesting to note that the trailing-edge coverts flutter at the downstream positions and extend the influence upstream to change the geometry and dynamics

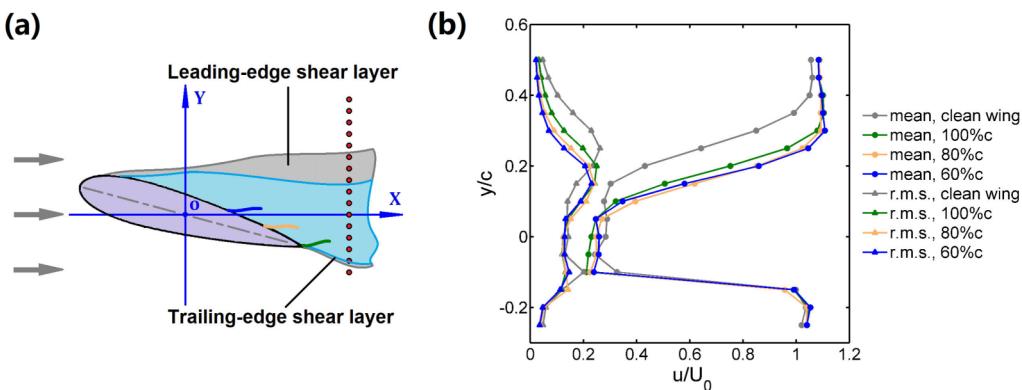


FIG. 6. (a) Schematic of the flow separation control effect by the trailing-edge coverts at the angle of attack of 15°. The cyan area represents the reduced wake and the gray area is the baseline. (b) Time-averaged velocity profiles (dots) and rms velocity distributions (triangles) of the “60%c,” “80%c,” “100%c,” and the clean wing cases.

TABLE II. Positions and peaks of the rms of the leading-edge (L.E.) and trailing-edge (T.L.) shear layers.

Test Case		L.E. position	T.E. position	L.E. rms	T.E. rms
Clean Wing		$y/c = 0.25$	$y/c = -0.1$	$u_{rms}/U_0 = 0.26$	$u_{rms}/U_0 = 0.20$
L.E. coverts	10% c	-0.1	-0.1	0.19	0.19
	20% c	0.05	-0.15	0.27	0.26
	40% c	0.15	-0.15	0.25	0.21
T.E. coverts	60% c	0.15	-0.1	0.23	0.14
	80% c	0.15	-0.15	0.24	0.14
	100% c	0.2	-0.1	0.25	0.13

of the leading-edge shear layer, which is worthy of further analysis in the dynamic perspective.

B. Coherence of shear layers

Figure 7 shows the power spectral density (PSD) of the turbulent fluctuations within the leading-edge and trailing-edge shear layers. The frequency is normalized by the incoming flow velocity and the chord length as the Strouhal number $St = fc/U_0$ for characterizing the unsteadiness of the separated shear layers. In the clean wing case, the leading-edge shear layer contains predominant peaks at the fundamental frequency $St \approx 0.2$ and the harmonic frequency $St \approx 0.5$, indicating the multiscale unsteady motions in the wake. These are the intrinsic frequency signatures of the flow separation for this high-angle-of-attack wing. Contrarily, in the 10% c case, the leading-edge shear layer is drawn to attach to the wall and merges itself with the trailing-edge shear layer. In particular, the peaks in the 10% c case were mostly smoothed in the spectrum, whereas the 20% c and 40% c cases are less effective. The changes of the spectra in the 10% c case suggest that the predominant unsteady motions are considerably attenuated by the fluttering covert near the leading edge and the wake flow is stabilized. As a result, the leading-edge coverts successfully

suppress the flow separation and furthermore, the adaptive perturbations attenuate the unsteady motions in the wake flow. Another benefit is that it is spontaneously activated only when the airflow around the wing becomes close to separation, for instance, during the bird perching, landing, and gliding in a gust of wind. Recent experiments [41] and numerical simulations [42] show that the flexible serrated coverts have effectiveness in flight drag reduction and noise reduction.

Further spectra in Fig. 8 show the significant change of the frequency signatures of the shear layers by applying the coverts at the three positions near the trailing edge, although the flow control effect is not as prominent as the leading-edge coverts. By comparing with the leading-edge spectra in Fig. 8(a), we find the coverts at the 100% chord length redistribute the turbulent kinetic energy from the low-frequency to the high-frequency components, resulting in a strong peak at the harmonic frequency $St \approx 0.5$. By applying the hot-wire probe within the trailing-edge shear layer, we find the coverts vibrate at the frequency of $St \approx 0.5$, which is driven by the airfoil separated from the trailing edge. As a result, the fluttering coverts at the trailing edge effectively suppress the generation of the large-scale structures and synchronize the leading-edge and trailing-edge shear layers at the harmonic frequency. In the following test the coverts at the 80%

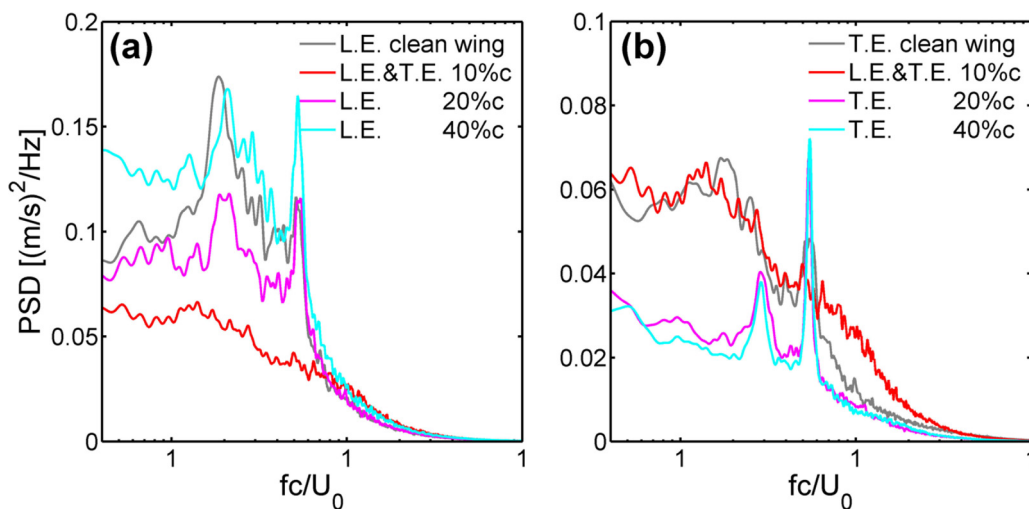


FIG. 7. Power spectral density of the shear layers in the 10% c , 20% c , 40% c , and clean wing cases, (a) within the leading-edge (L.E.) shear layers and (b) within the trailing-edge (T.E.) shear layers. Please note that in the 10% c case, the two separated shear layers merge into one, as denoted by “L.E.&T.E.” in the legends.

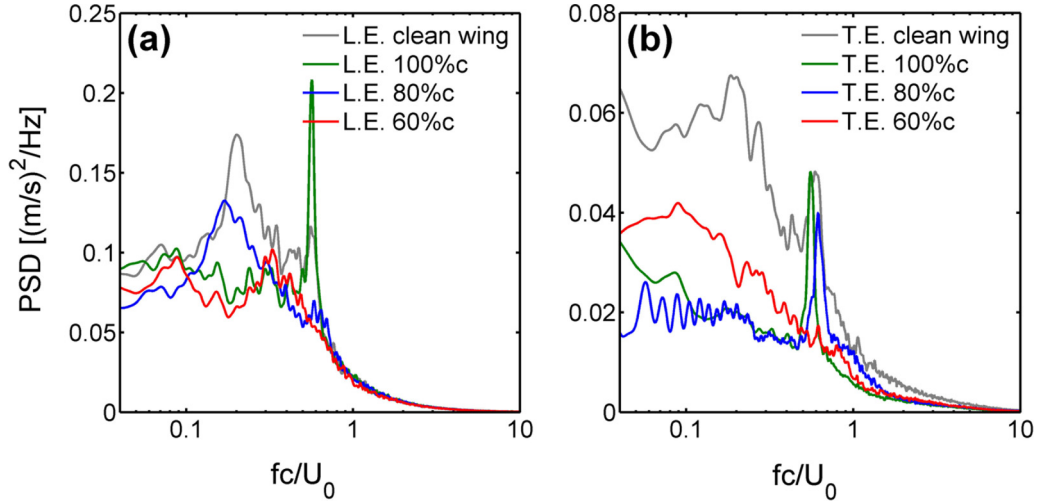


FIG. 8. Power spectral density of the shear layers in the 60%*c*, 80%*c*, 100%*c*, and clean wing cases (a) within the leading-edge (L.E.) shear layers and (b) within the trailing-edge (T.E.) shear layers.

chord length have the opposite redistribution effect in the leading-edge shear layer and concentrate the energy to the low-frequency components in a wide bandwidth at $St \approx 0.2$, while the trailing-edge shear layer still has the high-frequency peak at $St \approx 0.5$. It is interesting to note that the 80%*c* coverts activate a different dynamic mode of the leading-edge shear layer in which the fundamental peak is attenuated and the harmonic is suppressed. Furthermore, when the coverts are deployed at the 60% chord length, the leading-edge shear layer shows two wideband peaks at $St \approx 0.09$ and $St \approx 0.3$ with much lower magnitudes. By examining the trailing-edge shear layers, we find the coverts at 100% and 80% chord lengths both have the effect of concentrating the energy at the harmonic peak $St \approx 0.5$ and reducing the overall magnitudes in the spectra. In the 60%*c* case the trailing-edge shear layer contains no apparent peak in the whole frequency range. On the other hand, the double-peak frequency signature of the clean wing case shows different modifications by the coverts: the 100%*c* and 80%*c* deployments have the effect of strengthening the harmonic peak at $St \approx 0.5$ and the fundamental peak at $St \approx 0.2$, respectively, whereas the 60%*c* deployment suppresses both. It should be noted that these modifications differ from the reported reductions of the rigid flaps in the literature [22,25], showing that the flexibility of the flaps contributes an additional benefit of suppression of the separation bubble. It is therefore inferred that the flexible serrated coverts are capable of changing the flow structures in the separated shear layers as well as in the wake area, which may be an essential key to revealing the biophysical mechanism of high aerodynamic efficiency of bird wings [41,42].

The double-point measurement enables us to simultaneously obtain the velocity data from the leading-edge and trailing-edge shear layers. In order to quantify the interaction of the two separated shear layers, we calculate the magnitude squared coherence spectrum by

$$C_{xy}(f) = \frac{|P_{xy}(f)|^2}{P_{xx}(f)P_{yy}(f)}, \quad (6)$$

in which the term $P_{xy}(f)$ is the cross power spectral density based on the two simultaneous velocity data which are obtained by two hot-wire probes positioned within the leading-edge and trailing-edge shear layers, respectively. The coherence spectrum is used as a measure of quantifying the phase relationship between the leading-edge and trailing-edge shear layers in the frequency domain.

The comparisons in Fig. 9 show that the three positions of the trailing-edge coverts lead to different coherent features of the two separated shear layers. In particular, we find the strong coherence peak at $St \approx 0.5$ in the 100%*c* case, showing that the two shear layers flap in step in the high-frequency range due to the synchronization of the flutter coverts. However, as the coverts are deployed upstream to the 80% chord length, the coherence peak is suppressed. It is also worthy of note that, in the 60%*c* case, two coherence peaks are found at $St \approx 0.09$

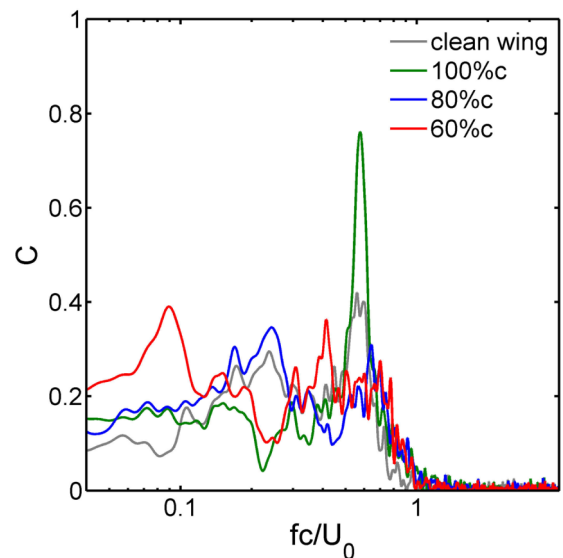


FIG. 9. Coherence of the leading-edge and trailing-edge shear layers in the 60%*c*, 80%*c*, 100%*c*, and clean wing cases.

TABLE III. The resolved frequencies of the discrete wavelet analysis.

Scale	Scaling Factor	Frequency [Hz]	Strouhal Number
1	2	2500	16.45
2	2^2	1250	8.22
3	2^3	625	4.11
4	2^4	312.5	2.06
5	2^5	156.3	1.03
6	2^6	78.1	0.51
7	2^7	39.1	0.26
8	2^8	19.5	0.13
9	2^9	9.8	0.06
10	2^{10}	4.9	0.03

and $St \approx 0.4$ as the multiscale coherent modes, resulting in effective reduction of the wake area and attenuation of the turbulent fluctuations. Thus, as the leading-edge shear layer is drawn downward closer to the trailing-edge shear layer, the two shear layers no longer flap independently but begin to interact with each other and coherently flap in step. This is the reason that the downstream perturbations extend the influence upstream to change the dynamics of the leading-edge shear layer. This effective deployment position is consistent with the direct observation that during the bird gliding and perching the lifted coverts are on the upper wing surface [10,12].

C. Amplitude modulation of small-scale turbulence

To analyze the scale interaction and arrangement of the shear layers under the influence of the fluttering coverts, we apply discrete wavelet transform to decompose the time series of velocity data into ten scale wavelet components in the frequency range from $f_s/2$ to $f_s/2^{10}$ as listed in Table III. Figure 10 provides an example of the wavelet coefficient contours derived from the leading-edge shear layers of the clean

wing and the 60%*c* cases. In the comparison, the unsteady characteristics of each frequency component are visualized in the time-frequency domain. The comparison shows the unsteady motions are attenuated in strength and they are shifted toward lower frequencies by the 60%*c* covert perturbations. As a consistent result with the PSD spectra in Fig. 8(a), the wavelet coefficients provide more detailed temporal information for each turbulent scale. We here define the large scales as the wavelet components from scale 7 to scale 10, while the small scales are defined as the wavelet components from scale 1 to scale 6. As the cutoff scale is set on scale 7 ($St \approx 0.26$), we therefore reconstruct the large-scale structures by the combination of scale 7 to scale 10 (denoted by \tilde{u}). These large-scale unsteady flapping motions within the shear layers are superimposed onto the turbulent background (denoted by u'). Taking advantage of the multiscale wavelet reconstruction [35], we can analyze the large-scale modulation effects on the different scales from scale 1 to scale 6, as well as the combination of them. By comparing the rms distributions of the individual wavelet scale 1, scale 5, and scale 6 in Fig. 11, we found that the reduction of turbulent fluctuations shows clear scale dependence, especially in the leading-edge shear layers at $0.15 < y/c < 0.25$. As the trailing-edge deployment position moves upstream, the most energetic components scale 5 and scale 6 are more effectively attenuated than the highest-frequency component scale 1. Contrarily, scale 1 is decreased within the low-speed wake area between the two shear layers. This scale dependence is consistent with the changes of the spectra in Fig. 8, suggesting that the coverts have a more beneficial effect of attenuating the most energetic flow structures. Moreover, it is also supported by the numerical simulation in the literature [25] that the flexible flaps induce more interaction between the LEV and TEV as the tip flutters back and forth, leading to effective stabilization of the wake flow.

By decomposing the turbulent fluctuations into the large-scale structures and small-scale turbulence, we calculate the

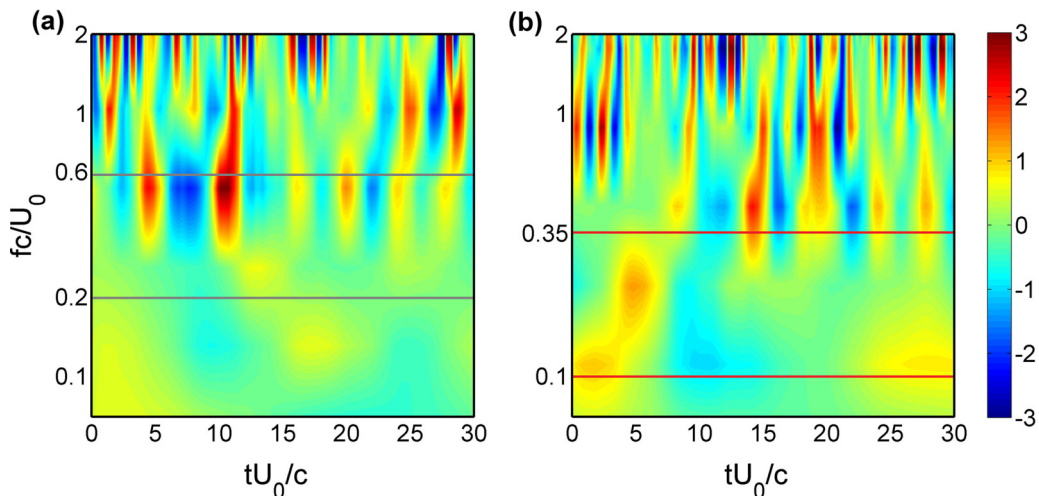


FIG. 10. Examples of the wavelet coefficient contours. (a) Measurement point at $y/c = 0.25$ within the leading-edge shear layer in the clean wing case. The gray lines indicate the peak frequencies of $St = 0.2$ and 0.6 in the spectrum. (b) Measurement point at $y/c = 0.15$ within the leading-edge shear layer in the 60%*c* case. The two red lines indicate the peak frequencies of $St = 0.1$ and 0.35 in the spectrum. Horizontal axis: the normalized time (only a segment of time is shown); vertical axis: the normalized frequency.

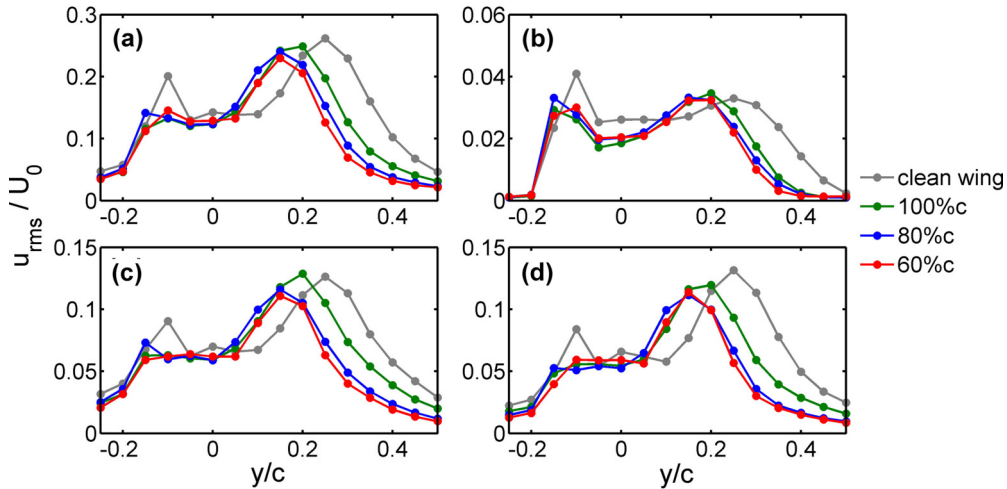


FIG. 11. The rms distributions of the wavelet components in the 60%c, 80%c, 100%c, and clean wing cases: (a) the measured data, (b) scale 1, (c) scale 5, and (d) scale 6.

large-scale amplitude modulation of the small-scale turbulence. In Fig. 12 the small-scale turbulence is replaced by the combined reconstructions from wavelet scale 1 to scale 6, as well as the individual scale 1, scale 5, and scale 6, respectively. One notable observation is that both the combinations and the individual scales are strongly modulated within the low-speed wake area ($-0.1 < y/c < 0.1$), and the modulation profiles are consistent with the shifting positions of the shear layers. In Fig. 12(b) there are increased plateaus of positive modulations of the smallest scale of turbulence in the wake area, which is also reported in the inner layer of turbulent boundary layer flows [35,38]. As the two separated shear layers are drawn closer to each other, the wake area in between is more influenced by the coherent separated shear layers. Meanwhile, the modulations of the most energetic components of scale 5 and scale 6 are clearly reduced within the leading-edge shear layer in the 80%c and 60%c cases, due to the suppression of the harmonic frequency of turbulent fluctuations.

On the other hand, there are completely opposite correlations outside of the wake area ($y/c < -0.2$ and $y/c > 0.2$). This phenomenon of the reversed modulation effects has also been discussed in turbulent boundary layer flows, in which the amplitude modulation is positive in the near-wall region ($y^+ < 10$) whereas it becomes negative in the buffer and logarithmic regions ($y^+ > 10$) [34,35,38,43]. As a key indicator for characterizing the coherent features in shear flows, the large positive profiles show the large-scale modulation of the small-scale turbulence within the low-speed wake area, whereas the negative profiles outside of the wake area are due to the intermittency of the bulk flow around the wing. Therefore we find the fluttering coverts attenuate the intermittency of turbulence outside the wake area ($y/c < -0.2$ and $y/c > 0.2$). Particularly, when fluttering at the 60% chord length, the coverts have the most effective flow control results of stabilizing the wake area and attenuating the intermittent flow around the wing.

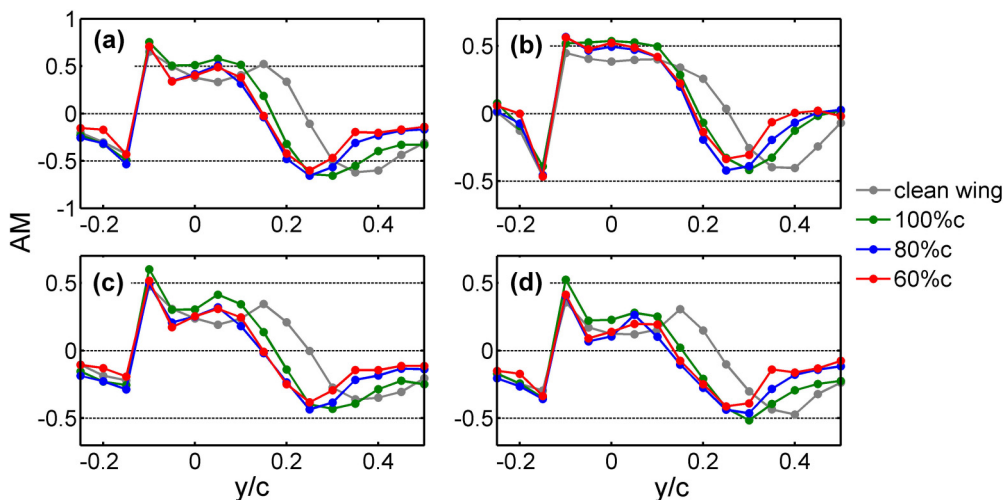


FIG. 12. The amplitude modulations of small-scale turbulence (u') by the large-scale structures (\tilde{u}). (a) \tilde{u} : combination from the wavelet scale 1 to scale 6; (b) \tilde{u} : scale 1; (c) \tilde{u} : scale 5; (d) \tilde{u} : scale 6. The large-scale structures are reconstructed from the wavelet scale 7 to scale 10.

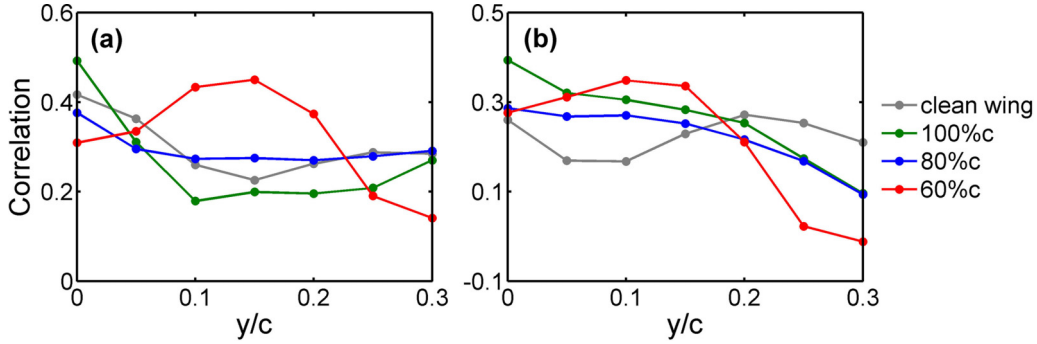


FIG. 13. Correlation of the leading-edge and trailing-edge shear layers: (a) cross-correlation coefficient of the large-scale structures of the leading-edge and trailing-edge shear layers $Coeff = \overline{u_{L.E.}' u_{T.E.}'}/\sqrt{\overline{u_{L.E.}'^2} \overline{u_{T.E.}'^2}}$; (b) leading-edge amplitude modulation on the trailing-edge turbulence $AM = \overline{u_{L.E.}' E_L(u_{T.E.}')}/\sqrt{\overline{u_{L.E.}'^2} [E_L(u_{T.E.}')]^2}$.

Furthermore, the two-point analysis provides a quantitative measure of the interaction of the leading-edge and trailing-edge shear layers. For clarity, the subscript “L.E.” refers to the moving probe across the leading-edge shear layer in the range of $0 \leq y/c \leq 0.3$, and the subscript “T.E.” refers to the fixed probe in the trailing-edge shear layer at $y/c = -0.1$. Therefore the cross-correlation of the large-scale structures of the two separated shear layers is obtained by

$$Coef = \frac{\overline{u_{L.E.}' u_{T.E.}'}}{\sqrt{\overline{u_{L.E.}'^2} \overline{u_{T.E.}'^2}}}, \quad (7)$$

in which the large-scale structures $\widetilde{u_{L.E.}'}$ and $\widetilde{u_{T.E.}'}$ are reconstructed from the wavelet scale 7 to scale 10. This correlation coefficient tracks the movements of the two separated shear layers in the reduced-order forms. Meanwhile, the leading-edge amplitude modulation of the trailing-edge turbulence is obtained by

$$AM = \frac{\overline{u_{L.E.}' E_L(u_{T.E.}')}}{\sqrt{\overline{u_{L.E.}'^2} \sqrt{[E_L(u_{T.E.}')]^2}}}, \quad (8)$$

where the small-scale turbulence $u_{T.E.}'$ is reconstructed from scale 1 to scale 6. This two-point modulation quantifies the large-scale modulation effect of the leading-edge shear layer on the small-scale turbulence of the trailing-edge shear layer.

In Fig. 13(a) we find a remarkable increase of the cross-correlation of large-scale structures of the two shear layers when deploying the coverts at the 60% chord length. This higher degree of correlation of the 60% case agrees well with the PSD spectra (Fig. 8) and the coherence spectra (Fig. 9), in which both the shear layers have the similar low-frequency peaks at $St \approx 0.09$ with a coherent feature. Moreover, in Fig. 13(b) we find a higher degree of modulation in the 60% case than other deployment positions and the clean wing case. This is solid quantitative evidence that the fluttering coverts at the 60% chord length synchronize the leading-edge and trailing-edge shear layers, resulting in an effective flow control result on the leading-edge flow separation phenomenon.

V. CONCLUSIONS

In order to reveal the aerodynamic role of the covert feathers on bird wings during high-angle-of-attack flights, we carry out wind tunnel experiments of the flexible, serrated, and featherlike devices deployed on the upper wing surface of the NACA 0018 airfoil model and measure the unsteady wake flow fields by single-probe and double-probe hot-wire anemometer. The artificial coverts are deployed at the various positions near the leading edge (10% c , 20% c , and 40%) and the trailing edge (60% c , 80% c , and 100% c), respectively. During the tests, the tips of the coverts are adaptively lifted and deflected by the separated airflow. The comparisons show that the leading-edge coverts successfully suppress the flow separation by adaptively fluttering the tips and generating small perturbations into the flow, resulting in a significantly reduced wake area with attenuated turbulent fluctuations. On the other hand, the fluttering coverts near the trailing edge induce the spectral coherence between the two separated shear layers, which therefore draw the two separated shear layers closer to each other and reduce the wake area as well. Although fluttering near the trailing edge, the coverts extend their influence upstream and suppress the generation of large-scale vortices and flapping motions in both shear layers. Particularly, the trailing-edge coverts at the 100% chord length redistribute the turbulent kinetic energy in the frequency domain, leading to concentrated spectral peak at $St \approx 0.5$ with a strong coherent feature. Furthermore, the multiscale analysis by the wavelet transform reveals that the trailing-edge coverts modify the interactions between different scales in terms of the large-scale modulation of small-scale turbulence. Among the three deployment positions, the coverts at the 60% chord length shows the most effective flow separation control result, which suppresses the fundamental and harmonic frequency components of the two shear layers and stabilizes the wake flow. This is supporting evidence that the naturally evolved covert feathers on bird wings play an important role during flights.

The experimental work provides a physical interpretation of the aerodynamic role of a single row of coverts on bird wings. However, the high aerodynamic efficiency under various complex flow conditions is a result from the combined effect of multiple rows of coverts on the wing surface, each

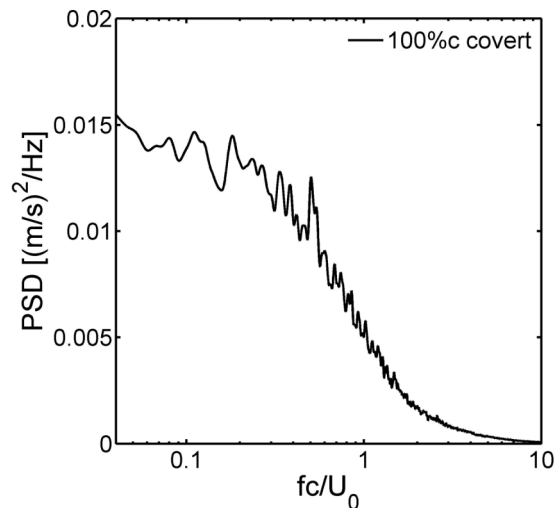


FIG. 14. Power spectral density of the perturbations of the trailing-edge coverts at the 100% chord length.

row of which is adaptively deflected by the local airflow. The systematic design of artificial coverts is worth further investigations for improving the aerodynamic efficiency of aircrafts.

ACKNOWLEDGMENTS

This research was supported by the National Natural Science Foundation of China (Grants No. 11902218, No. 11872272, No. 11972251, and No. 11732010), the Open Project Program of the Key Laboratory of Aerodynamic Noise Control (Grant No. ANCL20200105), and the Sino-German Center for Research Promotion-Mobility Program (Grant No. GZ 1575).

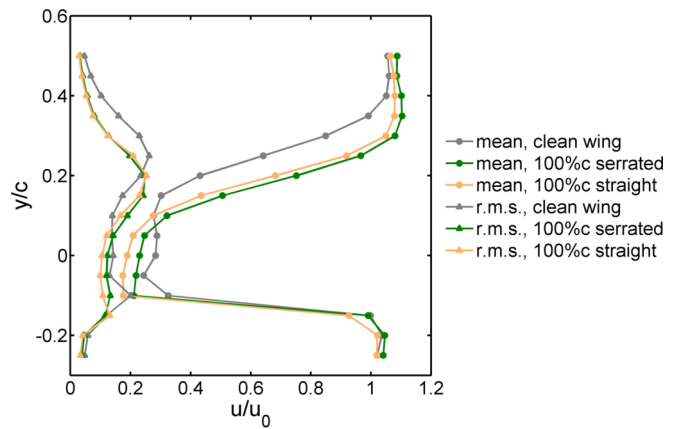


FIG. 15. The time-averaged velocity profiles (dots) and rms velocity distributions (triangles) of the clean wing, serrated-edge coverts at 100%c, and the straight-edge coverts at the 100% chord length.

APPENDIX

By positioning the hot-wire probe close to the covert tips (approximately 1 mm distance), we measured the 100%c trailing-edge covert's perturbations and show the power spectral density in Fig. 14. The perturbations are generated into the trailing-edge shear layer and lead to the spectral changes in Fig. 8(b).

For comparing the influence of the serration, we tested the straight-edge and serrated-edge coverts which were deployed at the 100% chord length. As shown in Fig. 15, we find the serrated edge has a slightly smaller wake flow area, more recovery of velocity deficit, and attenuated fluctuation peaks within the shear layers, which is mainly attributed to the serration making the covert lighter and more flexible to flutter in the unsteady flows than a rectangular type.

- [1] H. J. Willians, E. L. C. Shepard, M. D. Holton, P. A. E. Alarcon, R. P. Wilson, and S. A. Lambertucci, Physical limits of flight performance in the heaviest soaring bird, *Proc. Natl. Acad. Sci. USA* **117**, 17884 (2020).
- [2] B. G. Newman, Soaring and gliding flight of the black vulture, *J. Exp. Biol.* **35**, 280 (1958).
- [3] D. Lentink, U. K. Mueller, E. J. Stamhuis, R. de Kat, W. van Gestel, L. L. M. Veldhuis, P. Henningsson, A. Hedenstroem, J. J. Videler, and J. L. van Leeuwen, How swifts control their glide performance with morphing wings, *Nature (London)* **446**, 1082 (2007).
- [4] D. Lentink and R. de Kat, Gliding swifts attain laminar flow over rough wings, *PLoS ONE* **9**, e99901 (2014).
- [5] P. Henningsson, G. R. Spedding, and A. Hedenstroem, Vortex wake and flight kinematics of a swift cruising flight in a wind tunnel, *J. Exp. Biol.* **211**, 717 (2008).
- [6] L. Y. Matloff, E. Chang, T. J. Feo, L. Jeffries, A. K. Stowers, C. Thomson, and D. Lentink, How flight feathers stick together to form a continuous morphing wing, *Science* **367**, 293 (2020).
- [7] E. Chang, L. Y. Matloff, A. K. Stowers, and D. Lentink, Soft biohybrid morphing wings with feathers underactuated by wrist and finger motions, *Sci. Rob.* **5**, eaay1246 (2020).
- [8] T. Linehan and K. Mohseni, On the maintenance of an attached leading-edge vortex via model bird alula, *J. Fluid Mech.* **897**, A17 (2020).
- [9] J. J. Videler, E. J. Stamhuis, and G. D. E. Povel, Leading-edge vortex lifts swifts, *Science* **306**, 1960 (2004).
- [10] A. C. Carruthers, A. L. R. Thomas, and G. K. Taylor, Automatic aeroelastic devices in the wings of a steppe eagle *Aquila nipalensis*, *J. Exp. Biol.* **210**, 4136 (2007).
- [11] R. E. Brown and M. R. Fedde, Airflow sensors in the avian wing, *J. Exp. Biol.* **179**, 13 (1993).
- [12] D. W. Bechert, M. Bruse, W. Hage, and R. Meyer, Biological surfaces and their technological application - Laboratory and flight experiments on drag reduction and separation control, in *Proceedings of the 28th AIAA Fluid Dynamics Conference* (AIAA, Reston, VA, 1997), No. AIAA-97-1960.

- [13] T. Bachmann, J. Emmerlich, W. Baumgartner, J. M. Schneider, and H. Wagner, Flexural stiffness of feather shafts: Geometry rules over material properties, *J. Exp. Biol.* **215**, 405 (2011).
- [14] E. van Bokhorst, R. de Kat, G. E. Elsinga, and D. Lentink, Feather roughness reduces flow separation during low Reynolds number glides of swifts, *J. Exp. Biol.* **218**, 3179 (2015).
- [15] H. Zheng, F. Xie, Y. Zheng, T. Ji, and Z. Zhu, Propulsion performance of a two-dimensional flapping airfoil with wake map and dynamic mode decomposition analysis, *Phys. Rev. E* **99**, 063109 (2019).
- [16] Z. Li, L. Feng, J. Kissing, C. Tropea, and J. Wang, Experimental investigation on the leading-edge vortex formation and detachment mechanism of a pitching and plunging plate, *J. Fluid Mech.* **901**, A17 (2020).
- [17] G. Bramesfeld and M. D. Maughmer, Experimental investigation of self-actuating, upper-surface, high-lift-enhancing effectors, *J. Aircraft* **39**, 120 (2002).
- [18] R. Meyer, W. Hage, D. W. Bechert, M. Schatz, T. Knacke, and F. Thiele, Separation control by self-activated movable flaps, *AIAA J.* **45**, 191 (2007).
- [19] K. H. Kernstine, C. J. Moore, A. Cutler, and R. Mittal, Initial characterization of self-activated movable flaps, “pop-up feathers,” in *Proceedings of the 46th AIAA Aerospace Sciences Meeting and Exhibit* (AIAA, Reston, VA, 2008), No. AIAA-2008-369.
- [20] J. U. Schlueter, Lift enhancement at low Reynolds numbers using pop-up feathers, in *Proceedings of the 39th AIAA Fluid Dynamics Conference* (AIAA, Reston, VA, 2009), No. AIAA-2009-4195.
- [21] G. Allemand and A. Altman, Post-stall performance improvement through bio-inspired passive covert feathers, in *Proceedings of the 54th AIAA Aerospace Sciences Meeting* (AIAA, Reston, VA, 2016), No. AIAA-2016-2042.
- [22] D. Arivoli, I. Singh, and P. Suriyanarayanan, Rudimentary emulation of covert feathers on low-AR wings for poststall lift enhancement, *AIAA J.* **58**, 501 (2019).
- [23] J. Favier, A. Dauptain, D. Basso, and A. Bottaro, Passive separation control using a self-adaptive hairy coating, *J. Fluid Mech.* **627**, 451 (2009).
- [24] S. Klaen, T. Bachmann, M. Klaas, H. Wagner, and W. Schroeder, Experimental analysis of the flow field over a novel owl based airfoil, *Exp. Fluids* **46**, 975 (2009).
- [25] Z. Fang, C. Gong, A. Revell, G. Chen, A. Harwood, and J. O’Connor, Passive separation control of a NACA0012 airfoil via a flexible flap, *Phys. Fluids* **31**, 101904 (2019).
- [26] L. Wang, M. M. Alam, and Y. Zhou, Experimental study of a passive control of airfoil lift using bioinspired feather flap, *Bioinspiration Biomimetics* **14**, 066006 (2019).
- [27] K. Liu, H. Huang, and X. Lu, Hydrodynamic benefits of intermittent locomotion of a self-propelled flapping plate, *Phys. Rev. E* **102**, 053106 (2020).
- [28] P. B. S. Lissaman, Low-Reynolds-number airfoils, *Annu. Rev. Fluid Mech.* **15**, 223 (1983).
- [29] H. J. Goett and W. K. Bullivant, Test of N.A.C.A. 0009, 0012 and 0018 airfoils in the full-scale tunnel, NACA Technical Reports **647**, 97 (1939).
- [30] M. Farge, Wavelet transforms and their applications to turbulence, *Annu. Rev. Fluid Mech.* **24**, 395 (1992).
- [31] C. Meneveau, Analysis of turbulence in the orthonormal wavelet representation, *J. Fluid Mech.* **232**, 469 (1991).
- [32] T. Watanabe, Y. Sakai, K. Nagata, Y. Ito, and T. Hayase, Wavelet analysis of coherent vorticity near the turbulent/non-turbulent interface in a turbulent planar jet, *Phys. Fluids* **26**, 095105 (2014).
- [33] D. Simoni, D. Lengani, and R. Guida, A wavelet-based intermittency detection technique from PIV investigations in transitional boundary layers, *Exp. Fluids* **57**, 145 (2016).
- [34] Z. Tang, N. Jiang, X. Zheng, and Y. Wu, Local dynamic perturbation effects on amplitude modulation in turbulent boundary layer flow based on triple decomposition, *Phys. Fluid* **31**, 025120 (2019).
- [35] G. He, J. Wang, and A. Rinoshika, Orthogonal wavelet multiresolution analysis of the turbulent boundary layer measured with two-dimensional time-resolved particle image velocimetry, *Phys. Rev. E* **99**, 053105 (2019).
- [36] I. Daubechies, The wavelet transform time-frequency localization and signal analysis, *IEEE Trans. Inf. Theory* **36**, 961 (1990).
- [37] I. Daubechies, *Ten Lectures on Wavelets*, CBMS Lecture Notes Series (Society for Industrial and Applied Mathematics, Philadelphia, PA, 1991).
- [38] R. Mathis, N. Hutchins, and I. Marusic, Large-scale amplitude modulation of the small-scale structures in turbulent boundary layers, *J. Fluid Mech.* **628**, 311 (2009).
- [39] J. C. Lin, Review of research on low-profile vortex generators to control boundary-layer separation, *Prog. Aerosp. Sci.* **38**, 389 (2002).
- [40] X. Ma, R. Geisler, and A. Schroeder, Experimental investigation of three-dimensional vortex structures downstream of vortex generators over a backward-facing step, *Flow Turbul. Combust.* **98**, 389 (2017).
- [41] E. Sarradj, C. Fritzsche, and T. Geyer, Silent owl flight: Bird flyover noise measurements, *AIAA J.* **49**, 769 (2011).
- [42] J. W. Jaworski and N. Peak, Aerodynamic noise from a poroelastic edge with implications for the silent flight of owls, *J. Fluid Mech.* **723**, 456 (2013).
- [43] K. R. Sreenivasan, On the fine-scale intermittency of turbulence, *J. Fluid Mech.* **151**, 81 (1985).